Modeling of Crack Propagation in Thin-Walled Structures Using a Cohesive Model for Shell Elements

Pablo D. Zavattieri
GM Research and Development Center,
30500 Mound Road,
Warren, MI 48090-9055
e-mail: Pablo.zavattieri@gm.com

A cohesive interface element is presented for the finite element analysis of crack growth in thin specimens. In this work, the traditional cohesive interface model is extended to handle cracks in the context of three-dimensional shell elements. In addition to the traction-displacement law, a bending moment-rotation relation is included to transmit the moment and describe the initiation and propagation of cracks growing through the thickness of the shell elements. Since crack initiation and evolution are a natural outcome of the cohesive zone model without the need of any ad hoc fracture criterion, this model results in automatic prediction of fracture. In particular, this paper will focus on cases involving mode I/III fracture and bending, typical of complex cases existing in industrial applications in which thin-walled structures are subjected to extreme loading conditions (e.g., crashworthiness analysis). Finally, we will discuss how the three-dimensional effects near the crack front may affect the determination of the cohesive parameters to be used with this model. [DOI: 10.1115/1.2173286]

1 Introduction

The cohesive zone model (CZM) has gained significant importance in the modeling of crack propagation in solids in recent years. Although this model was first proposed by Barenblatt in 1962 [1] to describe material degradation and separation in a process zone in front of the crack tip in brittle materials and then applied to ductile fracture by Dugdale in 1959 [2], most of the advances in the implementation of this model into numerical methods have taken place during the last decade [3–7].

The most commonly used technique to incorporate the cohesive zone model into a finite element analysis is the discrete representation of the crack which is accomplished by introducing cohesive surfaces (or so-called zero-thickness interface elements) along interelement boundaries. In most cases, these special elements are governed by a cohesive constitutive law that relates the traction with the opening and shear displacement across the interface [3–7]. Although other techniques that make use of smeared or exact representation of the crack regardless of the initial mesh have been developed in the last few years [8–10], the utilization of interface elements remains attractive essentially due to the simplicity and effectiveness in some applications. In fact, the main advantage is that the complexity of crack initiation and evolution (including branching, coalescence, and arrest) can be modeled as a natural outcome of the model, without the need of any additional fracture criterion.

The first efforts to extend these cohesive models to fully three-dimensional problems were made by Ortiz and co-workers [11,12]. Thereafter, similar works have found this tool to be highly predictable of different kinds of three-dimensional problems [13,14]. However, there is a set of problems involving thin-walled structures (such as the analysis of thin plates, fuselage, sheet-metal forming, and crashworthiness) where the use of 3D solid elements would be prohibitive from the computational viewpoint. Generally, these engineering problems are solved with shell or other structural elements [15]. Li and Siegmund [16] made the first attempt to extend the cohesive zone model for shell elements. In their work, crack propagation under mode I/III conditions was studied in aluminum panels. However, the out-of-plane bending deformation was not contemplated in their cohesive model. It should be mentioned that, although the extension of the three dimension cases is relatively simple, shell elements present the challenge of having additional degrees of freedom (i.e., nodal rotations), which may help to identify other failure modes, such as surface crack propagating through the thickness of shells under bending conditions. Most recently, during the review of this paper, a new cohesive approach was proposed by Cirak et al. [17] in which the fracture of thin shells, including the out-of-plane bending mode, was accounted for in the framework of Kirchhoff-Love theory using subdivision elements, where only the nodal displacements were needed for the shell formulation.

In this work, the cohesive interface model is extended to handle cracks in the context of three-dimensional shell elements. In addition to the traction-displacement law, a bending moment-rotation relation is included to transmit the moment and describe the initiation and propagation of cracks growing through the thickness of the shell elements. Unlike the work presented in [17], the cohesive model proposed in this paper is intended for shell elements based on the Mindlin theory (commonly used in several applications) in which the nodal rotations are used for the out-of-plane bending modes. The paper is organized as follows: The description of the interface cohesive element and the constitutive law is given in Sec. 2. Simulations of simple mode I/III crack propagation problems and bending configuration in a thin elastic plate are discussed in Sec. 3. Comparisons with 3D simulations using solid elements showed that the new cohesive model for shell elements can predict the same material response using the same cohesive parameters. A study of ductile crack propagation of elastic-plastic materials and how this affects the determination of the cohesive parameters is included in Sec. 4. It is shown that when the same cohesive parameters are used in the solid and shell models, the results are appreciably different. This is because shell

Contributed by the Applied Mechanics Division of ASME for publication in the JOURNAL OF APPLIED MECHANICS. Manuscript received June 2, 2005; final manuscript received December 23, 2005. Review conducted by G. C. Buscaglia. Discussion on the paper should be addressed to the Editor, Prof. Robert M. McMeeking, Journal of Applied Mechanics, Department of Mechanical and Environmental Engineering, University of California—Santa Barbara, Santa Barbara, CA 93106-5070, and will be accepted until four months after final publication of the paper itself in the ASME JOURNAL OF APPLIED MECHANICS.

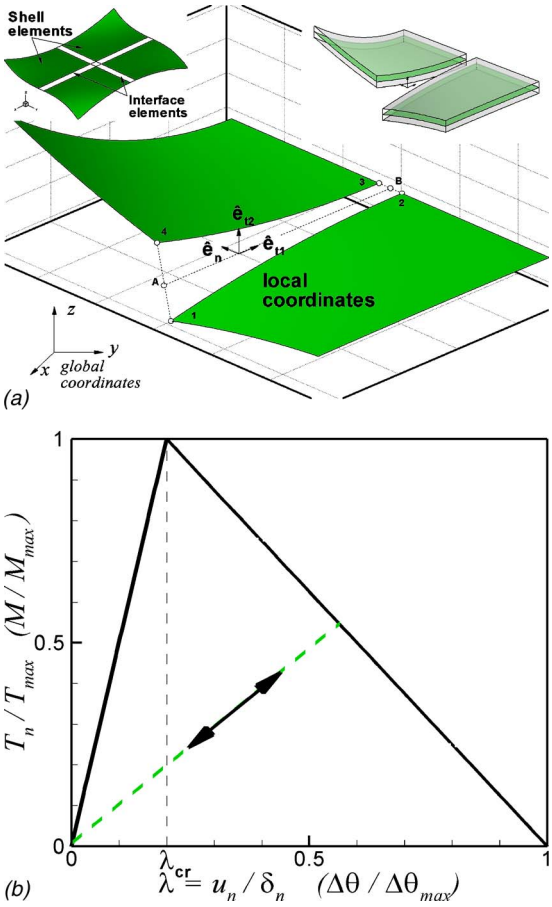

Fig. 1 (*a*) Schematics of the separation between two shell elements. The local coordinates are defined in the middle line of the interface elements. The upper-left box shows the cohesive interface elements embedded along quadrilateral shell elements (for illustration purposes, the shell elements have been separated). (*b*) Traction separation law for pure normal separation. The arrows indicate unloading and loading for $\lambda > \lambda_{cr}$. The same triangular law describes the bending moment-rotation relationship under pure rotation (denoted between parentheses).

elements cannot properly predict the three-dimensional deformational state ahead of the crack front that affects the overall behavior of the material. However, it is demonstrated that the cohesive zone model can still be used to represent this localized behavior by including a constitutive cohesive law that considers geometrical and material factors. A numerical technique to modify these cohesive laws to account for these effects is discussed in Sec. 4.1. Finally, a detailed analysis of the 3D cohesive zone reveals that the projection of the cohesive tractions and opening displacements lead to a well-defined "effective" cohesive law similar to those obtained by the numerical technique.

2 Model Description

2.1 Interface Elements for Shell Elements. The description for the formulation of the interface cohesive element for shell elements is based on the zero thickness four-node linear interface element described in previous works [6,7] extended to 3-D "*line*" interface elements connecting two quadrilateral shell elements. These interface elements are embedded along shell element boundaries as indicated in Fig. 1(*a*).

The model assumes that a perfect interface between two surfaces carries forces that oppose separation and shear between them until decohesion. From that point, the two surfaces will behave as distinct entities. The propagation of a crack can thus be simulated as the consecutive failure of interface elements. The cohesive relationship is expressed in terms of the opening displacement $\Delta=\{u_n,u_{t1},u_{t2}\}^T$ and the traction $\mathbf{T}=\{T_n,T_{t1},T_{t2}\}^T$, where the subscripts n, $t1$, and $t2$ denote the component of the traction and displacement in the direction of the local axes of coordinates. The magnitude of the opposing forces before debonding is a function of the relative normal and shear displacement jumps between the two surfaces, and this relationship is given by the constitutive cohesive law, $\mathbf{T}=f(\Delta)$. The interface between two shell elements is "intact" until the interface traction reaches a maximum value $T_{\max}$, and reduces to zero until the displacement jump reaches the maximum value. The reduction of cohesive traction can be interpreted as the progressive degradation of an otherwise intact stress state ahead of the crack tip. Details of the constitutive cohesive laws will be given in the following section.

This shell interface element should be compatible with the formulation of the shell element. In this work, the Belytschko-Lin-Tsay shell element [18] is considered. This shell element, which is the default shell element implemented in explicit finite element software DYNA3D [19], is widely used in several applications including crashworthiness and structural analysis. The formulation of this shell element uses the Mindlin theory of plates [20], which allows for transverse shear strains through the thickness of the plate, as well as thickness reduction. Since the displacements in a quadrilateral shell element can be approximated with classical C^0 interpolations, each node has six degrees of freedom, three translational, (x,y,z) and three rotational, $(\theta_x,\theta_y,\theta_z)$.

2.2 Constitutive Cohesive Law. In this work, the so-called triangular law introduced by Espinosa and Zavattieri [6,7] is extended to 3-D interface elements connecting quadrilateral shell elements. In formulating the cohesive law, a nondimensional effective displacement jump is defined by $\lambda=\sqrt{(u_n/\delta_n)^2+\beta_1^2(u_{t1}/\delta_{t1})^2+\beta_2^2(u_{t2}/\delta_{t2})^2}$, where u_n, u_{t1}, and u_{t2} are the actual normal and tangential displacement jumps at the interface estimated by the finite element analysis, and δ_n, δ_{t1} and δ_{t2} are the critical values at which the interface failure takes place.

Assuming a potential of the form $\Phi(u_n,u_{t1},u_{t1})=\delta_n T_{\max}(\lambda-\lambda^2/2)/(1-\lambda_{cr})$, then the components of the traction acting on the interface in the fracture process zone in the local configuration are given by

$$T_n=\frac{\partial\Phi}{\partial u_n}=\frac{\partial\Phi}{\partial\lambda}\frac{\partial\lambda}{\partial u_n}=\frac{1-\lambda}{\lambda}\left(\frac{u_n}{\delta_n}\right)\frac{T_{\max}}{(1-\lambda_{cr})}$$

$$T_{t1}=\frac{\partial\Phi}{\partial u_{t1}}=\frac{\partial\Phi}{\partial\lambda}\frac{\partial\lambda}{\partial u_{t1}}=\frac{1-\lambda}{\lambda}\left(\frac{u_{t1}}{\delta_{t1}}\right)\frac{\alpha_1 T_{\max}}{(1-\lambda_{cr})}$$

$$T_{t2}=\frac{\partial\Phi}{\partial u_{t2}}=\frac{\partial\Phi}{\partial\lambda}\frac{\partial\lambda}{\partial u_{t2}}=\frac{1-\lambda}{\lambda}\left(\frac{u_{t2}}{\delta_{t2}}\right)\frac{\alpha_2 T_{\max}}{(1-\lambda_{cr})} \quad (1)$$

where $\alpha_1=\beta_1^2(\delta_n/\delta_{t1})$ and $\alpha_2=\beta_2^2(\delta_n/\delta_{t2})$. λ is monotonically increasing and has the form $\lambda=\max(\lambda_{\max},\lambda)$ with $\lambda_{\max}=\lambda_{cr}$ at the beginning. Once the maximum traction is reached, the interface starts failing, the traction reduces to zero, and any unloading in the range $\lambda_{cr}<\lambda\leqslant 1$ takes place irreversibly. Once the effective displacement jump λ reaches or exceeds a value of 1, the interface element is broken and the crack is said to have initiated. Subsequent failure of neighboring interface elements leads to crack evolution. The most attractive feature of this new law is that this irreversible behavior is already incorporated in the law. Figure 1(*b*) shows the variation of the tensile cohesive traction $T_n/T_{\max}$ with respect to the nondimensional normal displacement. The area under the curve for normal traction in the absence of tangential traction gives the cohesive energy (work of separation) G_{Ic} for mode I, namely $G_{Ic}=\delta_n T_{\max}/2$. Similarly, the energies for modes II and III can be obtained as $G_{IIc}=\beta_1^2 G_{Ic}$ and $G_{IIIc}=\beta_2^2 G_{Ic}$, respectively. Once $\lambda\geqslant\lambda_{cr}$, the cohesive interface begins to irreversibly

dissipate energy defined as $G_{dis}=G_{Ic}(\lambda_{max}-\lambda_{cr})/(1-\lambda_{cr})$.

2.3 Fracture by Bending. In this section, a novel cohesive formulation that accounts for the effect of cracks growing through the thickness by bending is proposed. In addition to the traction-displacement law (Eq. (1)), a bending moment-rotation relation is included to transmit the moment and describe the initiation and evolution of cracks. In formulating this cohesive law, a nondimensional effective displacement jump is redefined by adding an extra term, $\lambda=\sqrt{(u_n/\delta_n)^2+\beta_1^2(u_{t1}/\delta_{t1})^2+\beta_2^2(u_{t2}/\delta_{t2})^2+\hat{\beta}^2(\Delta\theta/\Delta\theta_{max})^2}$. Since cracks are allowed to grow along interface elements, and assuming that the crack will grow in the direction of the maximum stress produced by bending, only the rotation θ_{t1} in the direction $\hat{\mathbf{e}}_{t1}$ (parallel to the middle line) will be considered.

Assuming the same potential of Sec. 2.2, the expressions of the normal and tangential tractions remain the same as in Eq. (1), except that λ has a contribution from the rotation and the bending moment is given by

$$M_{t1}=\frac{\partial\Phi}{\partial\Delta\theta}=\frac{\partial\Phi}{\partial\lambda}\frac{\partial\lambda}{\partial\Delta\theta}=\frac{1-\lambda}{\lambda}\left(\frac{\Delta\theta}{\Delta\theta_{max}}\right)\frac{\hat{\alpha}T_{max}}{(1-\lambda_{cr})} \tag{2}$$

where $\hat{\alpha}=\hat{\beta}^2(\delta_n/\Delta\theta_{max})$. Since $\hat{\beta}$ is nondimensional, $\hat{\alpha}$ has dimensions of length/radians and a maximum moment can be defined as $M_{max}=\hat{\alpha}T_{max}$. If there is only pure rotation along the axis $\hat{\mathbf{e}}_{t1}$, this bending moment-rotation relationship represents a nonlinear rotational spring carrying a moment that opposes the bending. Under theses circumstances, the cohesive law has the same triangular shape as the one shown in Fig. 1(*b*). The rising portion of the curve describes the elastic behavior of an intact shell and any loading/unloading takes place linearly with an initial bending stiffness given by $\kappa=M_{max}/(\lambda_{cr}\Delta\theta_{max})$. When the bending moment reaches a maximum value M_{max} a surface crack initiates and propagates through the thickness. Any unloading in the range $\lambda=[\lambda_{cr},1]$ will take place irreversibly with a bending stiffness lower than the initial value. That bending stiffness will decrease as the crack grows until the interface element *breaks* at $\lambda=1$.

In early works, the concept of including a rotational spring along shell element boundaries was introduced by Rice and Levy [21] and later extended to stationary elastic-plastic crack analysis by Parks and White [22]. In their work, the spring represents the additional compliance contributed by the presence of stationary part-through surface cracks. In this new model the same idea is applied in the context of the cohesive zone model, allowing the crack to propagate due to the bending moment and in-plane stresses.

3 Crack Propagation in Elastic Thin Panels

In this section, we will present a simple case of crack propagation in a precracked elastic thin panel under three different loading conditions: tension, torsion, and bending. The main purpose of this study is to compare the new cohesive model for shells with a fully three-dimensional model based on hexahedral continuum elements and their respective cohesive interface elements. Considering that the cohesive zone model has been successfully tested for solid elements in two and three dimensions [3–14], this comparison will allow us to determine how well the proposed model for shell elements is capable of predicting the same fracture behavior using less computational time.

The geometry of the precracked panel is presented in Fig. 2(*a*). The length of this panel is $L=30$ cm, the width $W=12.7$ cm, and thickness $t=6$ mm. The tensile axis is aligned with the y-direction and a crack of initial length $a_0=26$ mm lies along the line $y=0$. For all the cases, the specimen is simulated using both hexahedral and shell meshes (see Figs. 2(*b*) and 2(*c*)). The hexahedral mesh has been constructed using the same shell elements as base with four hexahedral elements through the thickness. The shell element selected is the Belytschko-Tsay shell with five integration points through the thickness. In this analysis, cohesive interface elements

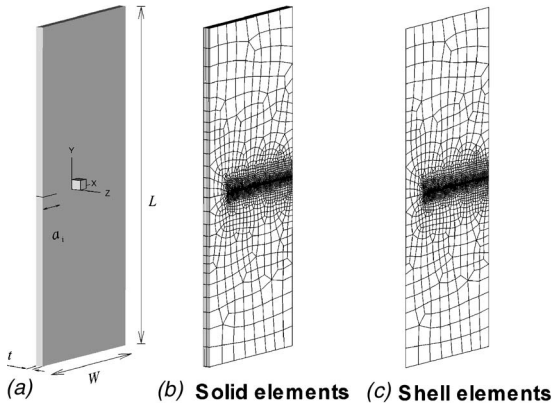

Fig. 2 (*a*) Geometry used for the crack propagation analysis of a precracked elastic thin panel under three different loading conditions: tension, torsion, and bending; (*b*) Hexahedral mesh. (*c*) Shell mesh.

are only embedded along the line $y=0$, so that the crack is constrained to grow along the initial crack line. Since the material used for these simulations (Steel C300) behaves in a brittle fashion, it is assumed that the crack will only grow under pure mode I and crack branching is not allowed. It should be mentioned that this kind of assumption is commonly used by several investigators [4,11,12,14,16,23]. The constitutive material parameters for steel C300 are $E=200$ GPa, $\nu=0.3$, $\rho=7830$ kg/m^3. The cohesive parameters are $T_{max}=700$ MPa, $\delta_n=\delta_{t1}=\delta_{t2}=70$ μm, $\beta_1=\beta_2=1.0$, and $\lambda_{cr}=0.3$. In addition to the condition that the element size has to be much smaller than the dimension of the block to provide an accurate representation of the stress near the crack tip, the cohesive element size should be also able to resolve the length over which the cohesive model plays a role in the elastic solution. For a simple cohesive law, under pure mode I conditions, Rice [24] proposed a simple expression of the cohesive zone length given by the elastic properties, and the cohesive parameters, $l_{cz}\approx(9\pi E/32)(G_{Ic}/T_{max}^2)$. Considering the material parameters for the case to be analyzed in this section, the cohesive zone length is $l_{cz}\approx 9$ mm. It is common practice to evaluate this characteristic length before the finite element meshes are built to ensure convergence in the results [5–7]. In addition to this, a convergence analysis with cohesive element size $L_e<l_{cz}$ was also performed. Finally, to satisfy all the length scales a cohesive element size of approximately $L_e=1$ mm was chosen. A similar convergence analysis was performed to determine the number of layers of elements needed through the thickness of the plate. It was then determined that for the elastic simulations presented in Secs. 3.1–3.3, five layers of elements through the thickness of the plate were sufficient. In this preliminary study, the material is treated as elastic, using the continuum elastic model for large deformations available in DYNA3D [19]. Discussion on elastic-plastic material is given in Sec. 4.

Cohesive interface elements connecting hexahedral elements: Similar to the case of shell elements, the formulation of the cohesive interface elements connecting the faces of two hexahedral elements is based on a zero-thickness eight-node bilinear interface element similar to that previously presented in [14]. Like in any traditional cohesive interface element for 2- and 3-D, only the displacement-traction relationship constitutes the cohesive law [3–7,11–14]. The components of the opening displacement are $\Delta=\{u_n,u_{t1},u_{t2}\}^T$, and the nondimensional effective displacement jump becomes $\lambda=[(u_n/\delta_n)^2+\beta_2^2(u_t/\delta_t)^2]^{1/2}$ where $(u_t/\delta_t)^2=(u_{t1}/\delta_{t1})^2+(u_{t2}/\delta_{t2})^2$. As a result, the cohesive law employed for these interface elements is the same as the one given by Eq. (1) considering $\delta_{t1}=\delta_{t2}=\delta_t$. The main difference between this cohesive law and the one proposed for the shell interface element in

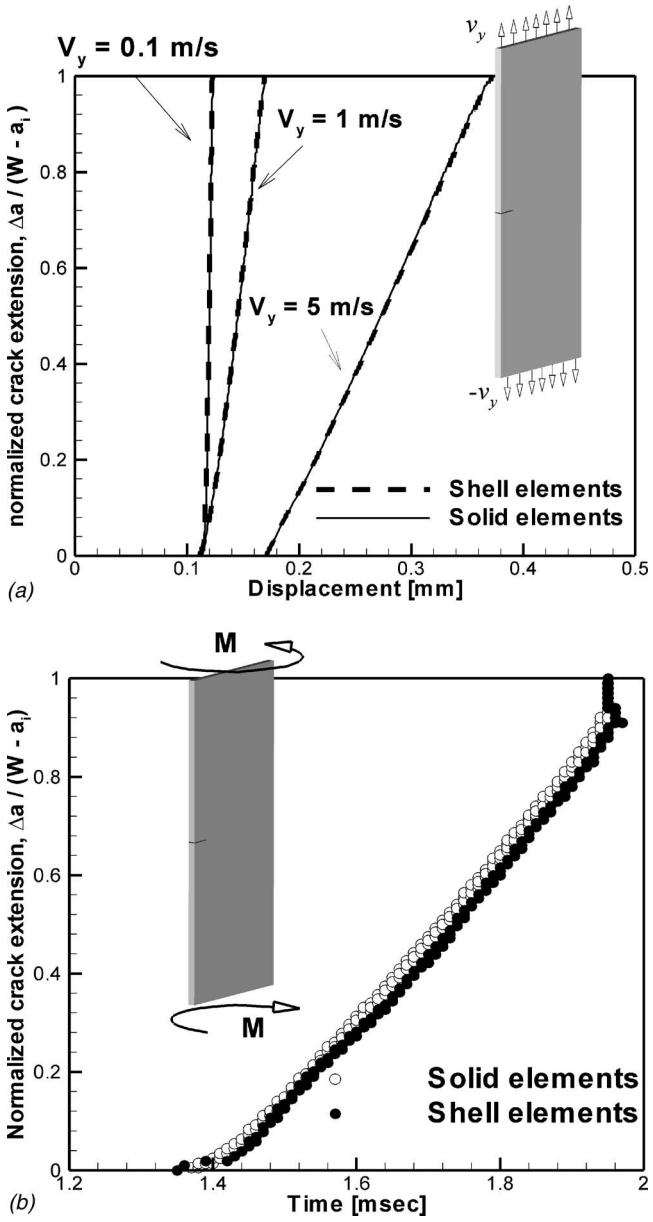

Fig. 3 (*a*) Tension test: crack tip position versus displacement for three different loading rates. (*b*) Torsion test: crack tip position as a function of time for the case where the elastic thin plate is loaded under mode III conditions.

Sec. 2.1 is that it is not necessary to make any difference between the tangential components.

3.1 Mode I Crack Propagation: Tension Test. In this case, the rectangular thin-walled specimen is subjected to dynamic tensile loading on both upper and bottom boundaries given by a uniformly applied velocity at the top and bottom boundaries, $v_y = \pm 0.1$, 1, and 5 m/s as shown in Fig. 3(*a*). The simulations were carried out until the crack reached the other end of the plate. An evaluation of the stress distribution, crack evolution, and force-displacement curves showed a good agreement between the fully three-dimensional model and the shell model.

Figure 3(*a*) shows the crack tip position as a function of the applied displacement for the three different loading rates. The crack tip position is determined by the global position of the integration point in which the condition $\lambda = 1$ is satisfied. In these figures the solid line represents the simulations with solids and the dashed line the simulations with shells. It is clear from these results that both models can predict exactly the same material response.

3.2 Mode III Crack Propagation: Torsion Test. To further test the model, the same specimen is simulated with solid and shell elements under torsion load. As in the previous case, the boundary conditions are only applied on the top and bottom boundaries, except that in this case a constant rotational velocity field of $\dot{\theta} = 0.08$ rad/s is applied. These geometry and loading conditions create a mode III stress field near the crack trip/front. The loading conditions and cohesive parameters are similar for both models. Given the asymmetric conditions at the crack plane, the moment-rotation relationship does not play an important role yet. However, this problem complements in some way the one considering only pure mode I. The results of these simulations are depicted in Fig. 3(*b*). The crack tip position as a function of time is similar for both cases. A closer examination of the middle plane in the solid case revealed that the stress field was similar to the one with shell elements.

3.3 Bending Test. In this case, the same precracked plate is loaded in a three-point bending setup. Unlike traditional setups to study crack propagation, in this specific problem the applied load is perpendicular to the plane of the plate such that out-of-plane bending is induced. The main idea behind this test is to provoke through-the-thickness crack propagation. The layout of this experiment is shown in Fig. 4(*a*). Two cylindrical rods are positioned under the plate, each one at 10 cm from crack plane. A third rod aligned with the crack plane is positioned just above the plate and it moves towards the plane with a constant velocity $v_z = 1$ m/s. The diameter of the rods is 1 cm. It was observed that one of the advantages of this setup is that the crack front propagates in two directions: (1) perpendicular to the plane of the plate, along the z-axis from the bottom to the top (through-the-thickness crack propagation) and (2) in the direction of the original crack along the x-axis, from the initial crack front to the other side of the plate (where the local axes are defined in Fig. 2). This leads to a more controlled crack growth, as opposed to the case without initial crack where the crack can grow through the thickness in an unrestrained mode. Although the shell model is not able to explicitly predict through-the-thickness crack growth, this configuration will test the capability of the model to predict the overall response of the structure.

As in previous cases, the cohesive parameters used for the shell model are the same as those used in the fully three-dimensional case. However, in this case the moment-rotation relationship of Eq. (2) becomes an important part of the overall constitutive cohesive law and, therefore, the cohesive parameters $\Delta\theta_{\max}$ and $\hat{\beta}$ need to be determined. Several simulations were performed with different parameters until a good match was achieved. Figure 4(*a*) shows the crack tip position as a function of time for best case with $\Delta\theta_{\max} = 0.05$ rad and $\hat{\beta} = 1.0$. In this figure, the crack evolution is represented by the x-coordinate of the centroid of the interface elements at the time where $\lambda = 1$ is satisfied. In the simulation with solid elements, several interface elements have the same x-coordinate. However, the time where the crack front passes through those points may be different. Figure 4(*a*) shows that the crack front evidently evolves differently along the various layers of elements. This confirms that the crack grows in two directions along the projected crack plane. Furthermore, it was observed that the crack initiates originally at the intersection of the initial crack front and the bottom surface and propagates to the upper surface as it grows in the x-direction.

A second configuration is tested to validate the model parameters. The thickness of the plate is reduced to 2 mm, and the impact velocity is increased to $v_z = 10$ m/s. The crack tip position as a function of time is shown in Fig. 4(*b*). Although the fully three-dimensional simulation case shows a strong through-the-

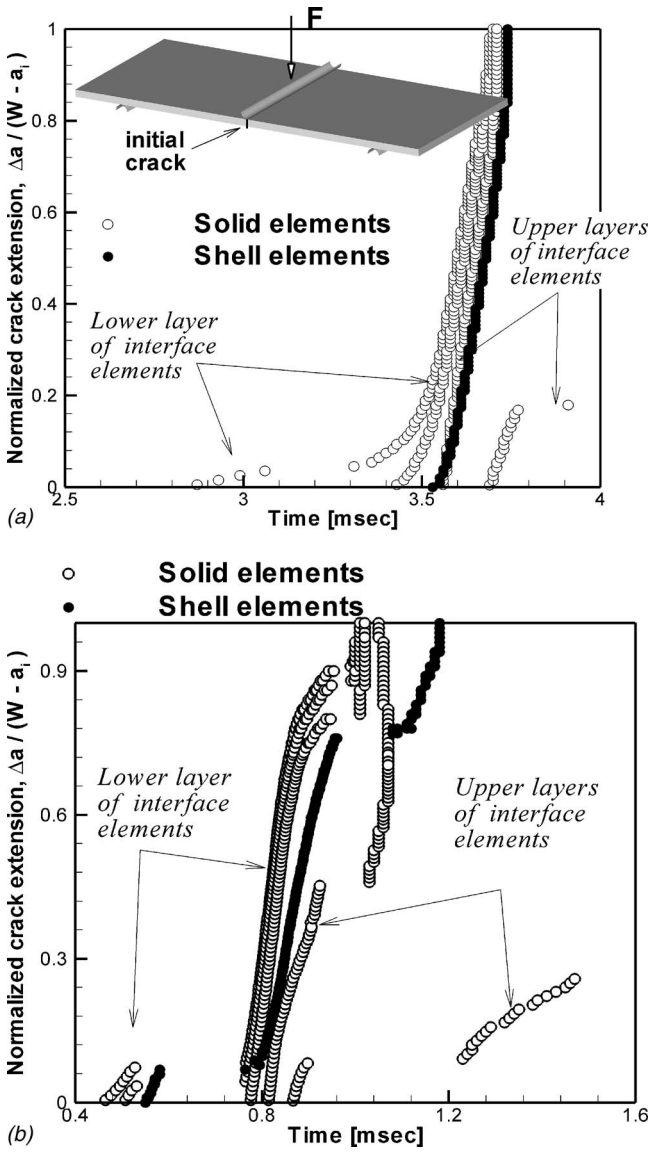

Fig. 4 Schematics of the three-point bending setup. (*a*) Crack tip position as a function of time for case with thickness t =6 mm and v_z=1 m/s. (*b*) Crack tip position as a function of time for the case with thickness t=2 mm and v_z=10 m/s. (Comment: The dots represent the x-coordinate of the centroid of the interface elements at the time where they fail. Clearly the simulation with solids shows the crack evolution in the different layers of elements.)

thickness crack propagation, the shell model is able to predict the crack propagation in the x-direction. Some of the discontinuities shown in these plots correspond to temporary arrests of the local crack front. The ability of the model with shell elements to capture such effects is remarkable. Moreover, it is observed that the overall force needed in the upper rod to break the plate is similar using both models.

The bottom views of the cracked plate and the stress field are shown in Fig. 5 for both models at three different times where the crack growth takes place. The position of the crack front/tip can be estimated from the stress field. It should be noted that the stress shown in the simulation with solid elements is that of the bottom surface of the plate, whereas the one shown in the case with shells represents the middle plane stress field. Therefore, the crack tip position of the model with shells as described in Fig. 4 can be considered as the position of the crack front at the middle plane.

4 Three-Dimensional Effects of Ductile Crack Propagation in Thin-Walled Specimens

The potential of the cohesive zone model to simulate crack propagation in elastic thin plates using shell elements has been examined in the last section. The material under consideration was only elastic, and in most cases the crack front was straight. Consequently, the plane stress formulation used by the shell elements may be suitable to model these kinds of problems. However, this desired behavior might not be observed in real ductile materials. The study of ductile fracture in elasto-plastic materials raises some concerns regarding the mechanical constraint imposed by the plastic deformation in the region near the crack front. Moreover, during ductile crack propagation of thin metals, a characteristic phenomenon called crack tunneling is observed. Crack tunneling occurs when the initially straight crack front grows more rapidly in the middle of the thin-walled specimen leading to the formation of rounded crack front profile. The plastic deformation around the tunneled crack front departures from the ideal deformational state observed in the elastic cases. As a consequence, additional out-of-plane components of shear stress become significant as the highly plastic deformation takes place near the crack region. In addition to crack tunneling, slant crack growth could also occur under certain conditions and materials. This is when the crack front turns into a 45 deg direction leading to a mixed mode I/III crack growth problem [25]. The study of slant fracture and its transition from flat crack is out of the scope of this analysis. Thus, we will restrict the current study to problems where crack fronts advance in flat mode.

All these complex mechanisms certainly affect the driving force of the crack and, consequently, the response of the material. It is then essential to make use of powerful tools that can accurately predict these localized phenomena. The cohesive zone model, in combination with the finite element method and continuum models, has proven to be a good choice for these kinds of analysis. Chen et al. [26–28] have extensively carried out fully three-dimensional analysis of crack growth in thick specimens using the cohesive model. Since ductile fracture in elasto-plastic materials is driven by void nucleation, growth, and coalescence, which are affected by the local constraint, they found a strong dependence of the cohesive parameters with the constraint conditions (stress triaxility), and as a result through-the-thickness variation of these parameters was considered. Moreover, they found that different cohesive parameters may be needed for different specimen geometries (i.e., double edge notched and compact test specimens). On the other hand, Roychowdhury et al. [14] have shown that for thin specimens, a three-dimensional model with constant cohesive parameters can fit the experimental results with good agreement, and yet were able to predict crack tunneling. Moreover, their work demonstrated the ability of the fully-three dimensional model to predict crack growth with different crack lengths and other geometries (including compact tests) with only one set of cohesive parameters.

The use of shell elements in conjunction with the cohesive model may require a special treatment to capture the fundamental nature of ductile crack propagation in thin specimens. Since shell theory is based on a bidimensional state of plane stress [15,20], all these three-dimensional effects mentioned in the previous paragraph are essentially ignored by the shell formulation, and any variation of thickness does not play any role in the simulated results [29]. It is then expected that the three-dimensional model and the shell model will lead to different results.

To illustrate the importance of the three-dimensional effect of tunneling in the crack region, an elasto-plastic specimen loaded in mode I is simulated with solid and shell elements. Details of this setup and material model are given later in Sec. 4.1. The same configuration is simulated with a pure elastic model for comparison purposes; however, the cohesive parameters are the same for all these simulations. Figure 6(*a*) compares the crack tip position as a function of the applied displacement for all these cases. Even

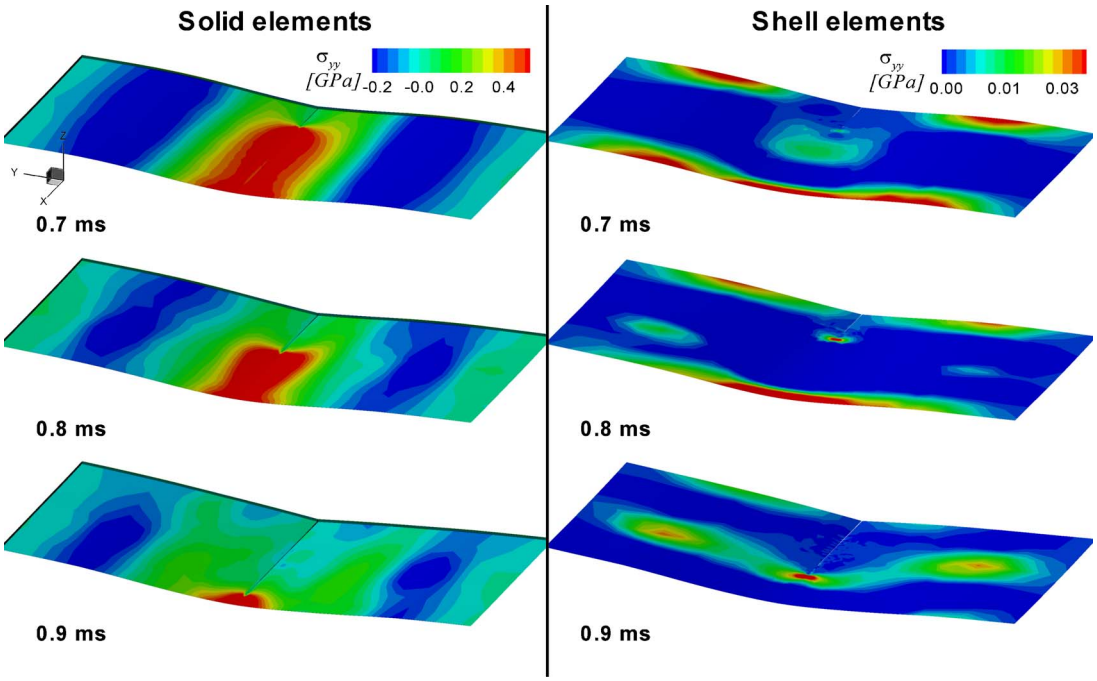

Fig. 5 Tensile stress σ_{yy} at different times during the propagation of the crack using a shell and solid mesh for the three-point bending configuration for t=2 mm and v_z=10 m/s.

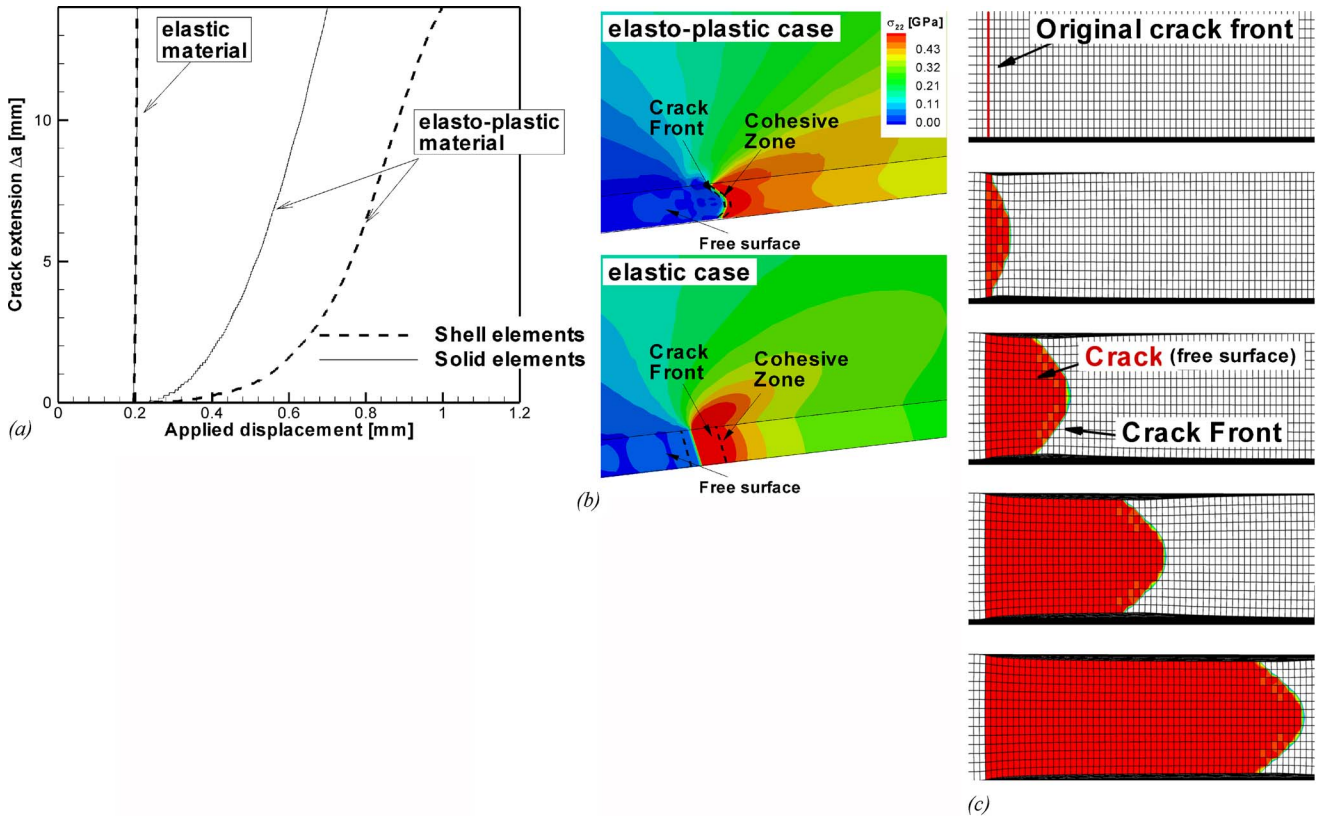

Fig. 6 (*a*) Crack tip position as a function of the applied displacement for a mode I ductile crack problem simulated with solid and shell elements. The solution for the solid mesh is given at the midsection of the panel. (*b*) Tensile stress field for the elasto-plastic and elastic material. (*c*) Details of the crack tunneling for the case modeled with 3D solid elements. The dark region indicates where G_{dis}/G_{Ic}=1.0.

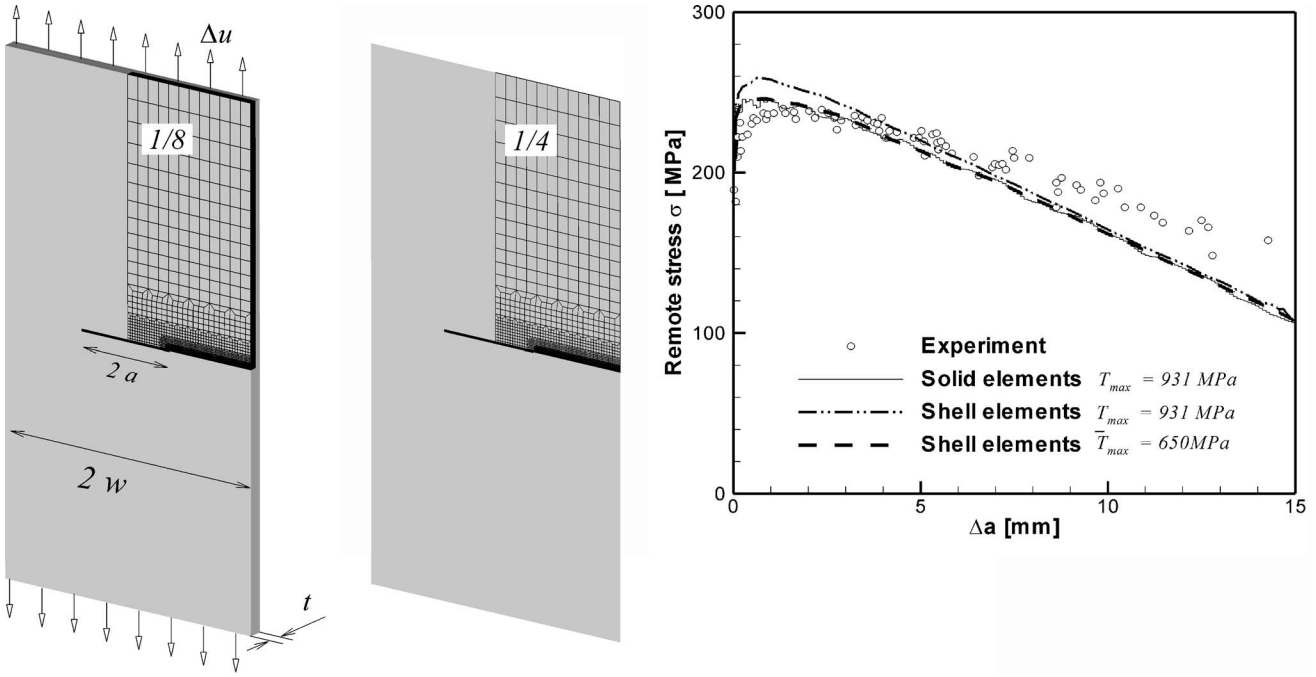

Fig. 7 (*a*) Details of the center-cracked aluminum panel. For simplicity purposes, the solid model considers only one-eighth of the geometry and (*b*) the shell model one-fourth. Symmetry boundary conditions are applied accordingly. (*c*) Predicted and measured load-crack growth response using both models (for comparison purposes the shell model uses two cohesive strengths).

though there is an excellent agreement when the material is elastic (as observed in Sec. 3.1), a noticeable disagreement in crack growth between the solid and shell model is obtained for the elasto-plastic case. Based on the hypothesis that the three-dimensional simulation contains the most reliable information about the true deformation process, there is clearly something missing in the model for shells. The three-dimensional tensile stress fields (σ_{yy}) for the elasto-plastic and pure elastic cases are shown in Fig. 6(*b*). For illustration purposes, only one half of the specimen from the crack plane is shown. The presence of a more complex three-dimensional stress state ahead of the crack front is evident in the elasto-plastic case. The same figure indicates the location of the crack front and the cohesive zone defined as the region where irreversible energy dissipation takes place $0 \leqslant (G_{\rm dis}/G_{\rm Ic}) < 1$ (see Sec. 2.2). Although not shown in this paper, the formation of "*shear lips*" caused by the plastic deformation on the free borders was also observed. Figure 6(*c*) shows the predicted crack front formation at different stages. The initial straight crack front evolves into a round-shaped crack front. The dark region indicates where the material has been totally separated (where $G_{\rm dis}/G_{\rm Ic}=1.0$). A thick black line on the free surfaces depicts evidence of thickness reduction.

Unfortunately, the localized three-dimensional deformational state near the crack front affects the overall response of the structure, and the bi-dimensional nature of the plane stress formulation is evidently not adequate to capture this phenomenon [29]. Nevertheless, it may still be possible to "*lump*" this localized behavior into the cohesive zone model. In this section, we will study this alternative by explicitly modifying the existing constitutive cohesive law to incorporate some geometrical and material factors that would eventually take into account the complexity of the tunneling effect. As an example, a mode I crack propagation experiment performed by Dodds and co-workers [23] on constrained center-cracked aluminum panel specimens will be used. It should be mentioned that, even though this experiment has been modeled with the cohesive zone model using both solid elements (Roychowdhury et al. [14]) and shell elements (Li and Siegmund [16]), both papers have reported different values of cohesive strength. This discrepancy will be discussed later in the section.

4.1 Analysis of a Center-Cracked Aluminum Panel. Following the work by Dodds and co-workers [14,23], simulations of an aluminum Al2024-T3 centered-crack panel are performed with the fully three-dimensional model. Following the description of Fig. 7(*a*), the width of the panel is $2w=75$ mm. The initial crack length is $a/w=0.333$ and the thickness of the plates is $t=2.3$ mm. Due to the symmetry of this configuration only one-eighth of the geometry is simulated. Thus, symmetry boundary conditions are employed accordingly. Cohesive elements are inserted in the projected crack plane/line. The element size in the fracture region is $L_e=0.1$ mm in the crack direction and $L_t=0.16$ mm in the thickness direction. This provides seven layers of elements across half-thickness. Mesh convergence studies performed by Dodds [14] demonstrated that $L_e=25$ mm and five layers of elements across the half-thickness were sufficient refinement to capture proper crack growth and tunneling formation. Due to the localized high plastic deformation ahead of the crack front, a convergence analysis was performed to evaluate the different element formulations to check for hourglass modes and undesired locking. Finally, it was found that, either, the fully integrated eight-node hexahedral elements using the mean dilatation method or the reduced integration hexahedral with stiffness form of the Flanagan-Belytschko hourglass method [19] could be safely used for this kind of analyses. Both formulations gave essentially the same results and were compared with the results reported by previous works and experiments [14,23].

In order to simulate the quasi-static test with displacement control loading using an explicit code such as DYNA3D, uniform low velocities are applied at the nodes on the top boundary. Previous calculations demonstrated that applied nodal velocities of about 500–750 mm/s were slow enough to prevent inertia effects in the calculation and satisfactorily fast to improve CPU efficiency. For the continuum material, the traditional isotropic elastic-plastic constitutive model that uses the Mises yield criterion is utilized. The elastic parameters for the Al2024-T3 are $E=71.3$ GPa and

$\nu=0.3$. The initial yield stress is $\sigma_y=345$ MPa and the plastic regimen is governed by $\sigma=\mathbf{K}\varepsilon^n$, where $\mathbf{K}=\sigma_y(E/\sigma_y)^n$, $n=0.1$ is the hardening exponent, σ is the true effective stress, and ε is the logarithmic strain. A systematic and parametric study performed by Roychowdhury et al. [14] led to the following calibrated cohesive parameters: $T_{\max}=2.7\cdot\sigma_y=931.5$ MPa and $G_{\mathrm{Ic}}=19$ kJ/m^2 (equivalent to a material toughness of $K_{\mathrm{Ic}}=38.5$ MPa$\sqrt{m}$). Figure 7(*c*) shows a good agreement between the numerical predictions and the experimental load-crack extension data. The simulation with shells will be discussed later.

Simulation with shell elements: Following the same scheme, the specimen is simulated with quadrilateral shell elements. In this case only one-quarter of the geometry is modeled with shells. As shown in Fig. 7(*b*), the shell mesh utilized is identical to one of the faces of the fully three-dimensional case. Keeping the same element size, the number of elements is therefore reduced from 21,700 solid elements and 1750 *plane* cohesive elements to only 3500 shell elements and 250 *line* cohesive elements. However, results using the same cohesive parameters as those used in the three-dimensional case are markedly different. Crack propagation is slower than in the real case and the applied peak force is significantly overpredicted. Figures 7(*c*) and 8(*a*) show the crack extension and normal applied force for the three-dimensional case and the shell simulation. The same effect has been observed in later simulations with specimens of different thicknesses. As expected, the fully three-dimensional simulations show a strong dependency of the overall material behavior with the specimen thickness, whereas the shell model predicts the same behavior; that is, the remote applied stress and crack extension are independent of the specimen thickness. It is clear that the cohesive law needs to be modified in order to take into account the three-dimensional effect that the shell elements cannot provide.

Calibration of the shell model: As mentioned before, Li and Siegmund [16] demonstrated that the cohesive zone model could certainly be used with shell elements to model these kinds of problems. Nevertheless, they reported a much lower value for the cohesive strength ($\bar{T}_{\max}=2\sigma_y$). Prior works on dynamic crack growth in thin sheets also led to similar findings [30]. This indicates that possible modifications of the cohesive zone model can involve a reduction of the cohesive strength. However, to the best of the author's knowledge, there is no work done on defining some sort of scaling law to relate the cohesive strength, $T_{\max}$, used in the three-dimensional calculations with the "modified" cohesive strength, $\bar{T}_{\max}$, for a 2D formulation. As previously discussed, the cohesive strength used in 3D simulations was shown to predict well different specimens and loading conditions [14]. On the other hand, the modified cohesive strength for shell elements should eventually contain information of the geometry and is expected to vary for different specimen thicknesses.

Looking at this trend, a series of numerical simulations with shell elements was performed for various values of the cohesive strength, $\bar{T}_{\max}$, and keeping the same cohesive energy G_{Ic} (the critical displacement is then computed as $\delta_n=2G_{\mathrm{Ic}}/\bar{T}_{\max}$). Figures 8(*a*) and 8(*b*) show the crack extension and force as a function of the remote applied displacement for different values of $\bar{T}_{\max}$ using the shell model. It is observed that crack growth is delayed for higher values of $\bar{T}_{\max}$. Conversely, the peak force increases with $\bar{T}_{\max}$. In conclusion, it was found that, with $\bar{T}_{\max}=1.88\ \sigma_y=650$ MPa, the shell model gives similar results to the three-dimensional model. The force-crack extension curve was also included in Fig. 7(*c*) using $\bar{T}_{\max}=931.5$ and 650 MPa for comparison purposes. This value is closer to Li and Siegmund's findings [16].

Certainly, this change in the value of $\bar{T}_{\max}$ is an "adhoc" modification of the cohesive law to take into account the three-dimensional effects for this specific thickness and material; hence,

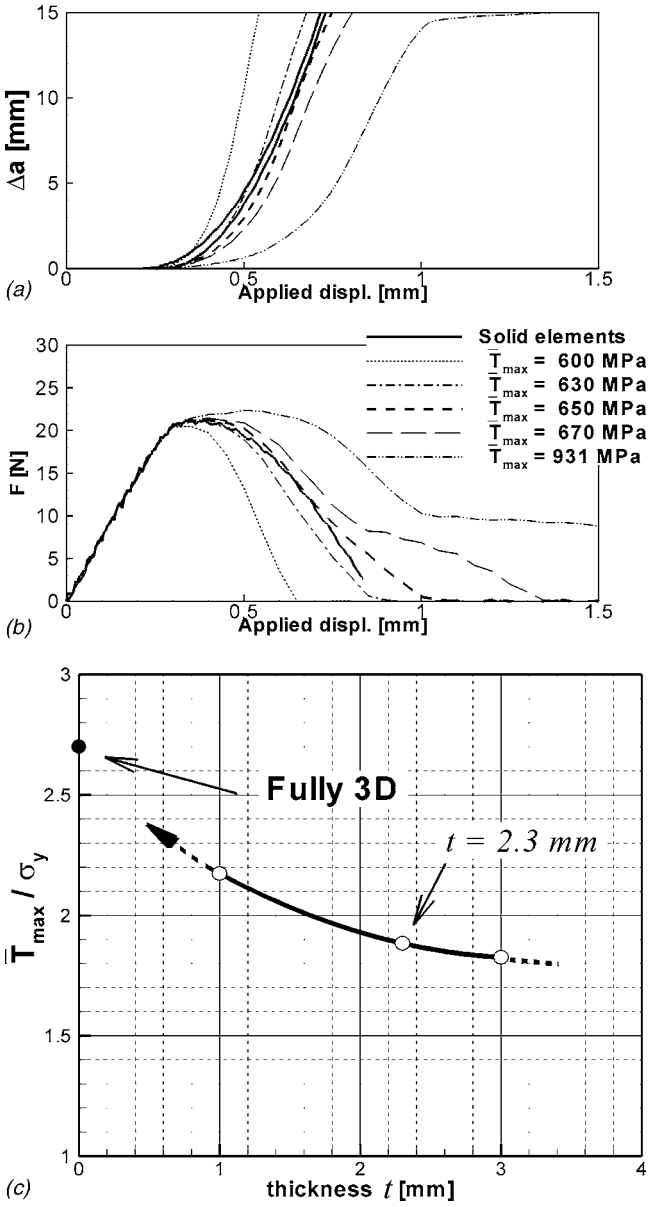

Fig. 8 (*a*) Crack extension and force as a function of the uniformly applied displacement obtained with the fully-three-dimensional model and with the shell model using different cohesive strength values. The two solid lines indicate the crack front position at the middle and outer surface of the specimen for the solid mesh with thickness $t=2.3$ mm. (*b*) Correction of the cohesive strength for shell elements as a function of the specimen thickness.

it should be expected that this correction would be different for other thicknesses or material (different values of E,ν,σ_y,n). Therefore, two more three-dimensional simulations were added for two more thicknesses, $t=1$ and 3 mm using the constant cohesive parameters $T_{\max}=931.5$ GPa and $G_{\mathrm{Ic}}=19$ kJ/m^2 used in [14]. Then, the same process was repeated for these two new specimens. Again, simulations with the shell model were performed for different values of $\bar{T}_{\max}$ for the two cases until good agreement was achieved. Finally, the best match was attained with $\bar{T}_{\max}=2.17\cdot\sigma_y$ for $t=1$ mm, and $\bar{T}_{\max}=1.82\cdot\sigma_y$ for $t=3$ mm. Figure 8(*c*) shows the best match $\bar{T}_{\max}$ versus the specimen thickness. This clearly demonstrates that the cohesive model for shell elements is affected by the geometry, at least for the modeling of

cracks under normal opening.

It should be mentioned that, although it is common practice to report only the force versus crack extension curves for these kinds of experiments (Fig. 7(*c*)), the individual evolutions of these two variables with respect to the applied remote displacement (Fig. 8(*a*)) are more sensitive to the cohesive parameters than just the combination of the two. Therefore, the two curves should be used simultaneously for calibration and validation purposes.

It should be repeated that this model is based on the assumption that the three-dimensional simulations give the best match to the experimental results, and the cohesive law proposed in this section is primarily an "adhoc" modification to modify crack growth under plane stress conditions to obtain an accurate response of the material. Certainly this modification can only take place whenever the three-dimensional model can accurately represent the experimental data in thin plates (where the crack extension and dimensions of the plate are much larger than the thickness of the plate). Extensions of this model can also be done for thicker plates if the right set of cohesive parameters is known for the three-dimensional model, even if these parameters vary with the local position with respect to the middle plane of the specimen, as found in [26–28]. However, in those cases where the cohesive parameters need to be changed for different specimens and boundary conditions in the 3D model, as in [27], the cohesive parameters will need to be changed for the shell model as well.

"Effective" cohesive law: Another way to look at this problem is by analyzing in detail the three-dimensional deformational state and extract from the calculations useful information that can eventually provide some guidelines to define a cohesive law for shell elements. Thus, it can then be possible to look at the bi-dimensional solution as a projection of the three-dimensional case. For instance, the three-dimensional cohesive zone ahead of the mode-I crack front, defined by the normal cohesive traction, is shown in Fig. 9(*a*) (upper corner). The maximum traction (when $T_n=T_{\max}$) follows a curved shape similar to the tunneled crack front. The same figure shows the profile of the normal traction along the x-axis in the direction of the crack growth. Data points represent the normal traction at each integration point of the three-dimensional calculation. The average *through-the-thickness* cohesive traction can be easily obtained by $\bar{T}_n=2/t'\int_0^{t'/2}T_n dz$ (shown as solid line), where $t'=t'(x)$ is the current thickness. The averaged maximum traction is then defined as $\bar{T}_{\max}$, which is notably lower than the cohesive strength used in the three-dimensional simulations. It was observed that this profile, as well as $\bar{T}_{\max}$, remains constant as the tunneling is fully developed and cracks propagate steadily. Three-dimensional simulations of different thicknesses reveal that this averaged maximum traction decreases for thicker panels.

Conversely, the opposite effect was found with the averaged normal opening (defined as $\bar{u}_n=2/t'\int_0^{t'/2}u_n dz$), in which the averaged maximum critical displacement is greater than the one used in the three-dimensional simulations and increases with the thickness of the panel. More remarkable is the combination of these two variables. Figure 9(*b*) shows the relationship between $\bar{T}_n$ and $\bar{u}_n$. Each dot represents the values at integration points of the plane cohesive elements at various stages of the crack propagation simulation. This well-defined "effective" cohesive law is shown for three thicknesses $t=1$, 2.3, and 3 mm. The original cohesive law ($T_{\max}=931.5$ MPa and $G_{\mathrm{Ic}}=19$ kJ/m^2) is also shown in dashed lines. Even though the shape of the cohesive laws departs from the original triangular shape, the overall cohesive energy does not deviate significantly from its original value, which confirms the assumption used in the previous section of keeping the same energy and only modifying the cohesive strength. In all the cases, the initial stiffness also remains unchanged. Consequently, these cohesive laws were implemented for shell elements, and simulations for each thickness were performed. Although, a similar trend to that described in the previous section was observed, the crack extension and applied force were not as accurate as the results obtained with the "calibrated" cohesive parameters. One possible explanation is that the averaged cohesive parameters are slightly greater than those obtained in the calibration process and, hence, do not take into consideration the real three-dimensional character of crack growth by only projecting in a 2D plane. However, this "effective" cohesive law provides some qualitative insight into the real mechanisms that need to be applied in order to define cohesive laws that can be compatible with a plane stress formulation.

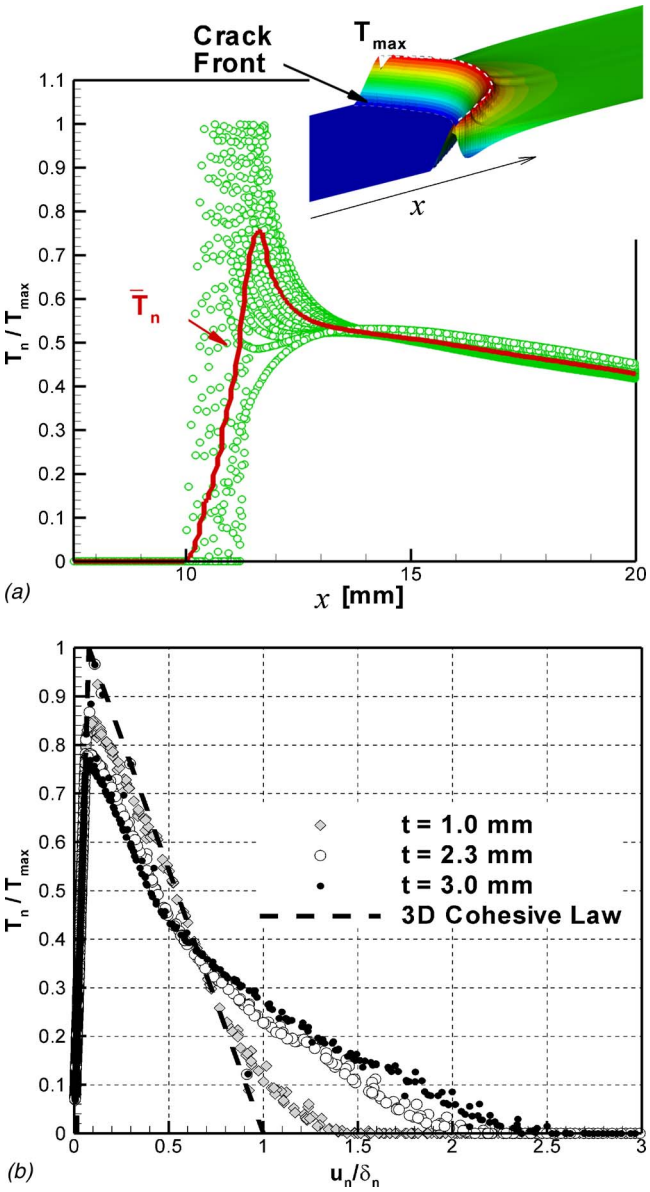

Fig. 9 (*a*) Normal cohesive traction profile developed near the crack front. Each dot represents the value at each integration point and its *x*-coordinate (initial straight crack front is located at *x*=0). The solid line represents its average through the thickness $\bar{T}_n$. (*b*) Effective cohesive law ($\bar{T}_n$ vs. $\bar{u}_n$) for three different specimen thicknesses.

5 Conclusions

In this paper, a three-dimensional finite-deformation cohesive element for shell elements for the finite element analysis of crack propagation in thin-walled structures was presented. A numerical

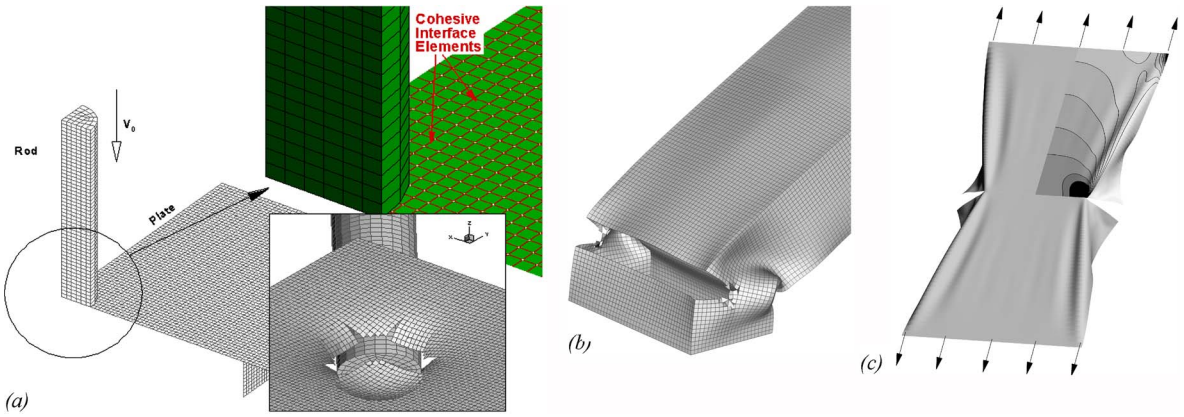

Fig. 10 (***a***) **Rod impacting a brittle plate.** (***b***) **Bending of an aluminum tube.** (***c***) **Fracture of polymer membranes.**

analysis for elastic thin plates was included to assess the capability of the model to predict crack growth under mode I/III and bending loading conditions. Unlike previous models [16], the proposed model incorporates a bending moment-rotation relation to transmit the moment and describe the initiation and propagation of cracks growing through the thickness of the shell elements. In addition, three-dimensional simulations of ductile crack propagation in elasto-plastic materials were used to emphasize the importance of plastic constrain in the region near the crack front. This numerical analysis suggested that the two-dimensional nature of plane stress shell elements together with the cohesive model may not be appropriate to accurately predict the three-dimensional deformational state ahead of the crack front that evidently affects the overall behavior of the material. Therefore, the cohesive law for shells needs to be modified to take into account these geometry and material factors. For that reason, a scaling law for the cohesive strength is proposed in this work (see Fig. 9). Future directions will be focused into a dimensional analysis where different geometry, as well as material parameters, will be included. Along these lines, it will be possible to come up with a dimensionless function for the "modified" cohesive strength as $\bar{T}_{\max}/\sigma_y = \Pi(t/l, E/\sigma_y, n, T_{\max}/\sigma_y)$, where the thickness t may be normalized by the ligament size (l) or the plastic zone length (Γ_p).

The versatility and ability of the model to predict crack growth under various loading conditions have been demonstrated in this work. This opens a new set of possible solutions for problems involving fracture in thin-walled structures that otherwise could not be solved with other models, such as dynamic impact and penetration of plates, deformation, and failure of tubes and tearing of membranes. Figure 10 shows some preliminary simulations performed with this model for various materials.

Finally, the limitations of this model were discussed in Sec. 4. The model is shown to work under the particular circumstances described in Sec. 4 and, clearly, a comprehensive and systematic dimensional analysis to determine clear limits of this model in terms of the geometric and material parameters (including the thickness and plastic zone size) is required, and further studies will be needed in future research works.

Acknowledgment

The author would like to thank Marcos Actis, Alejandro Patanella, and the Departmento de Aeronautica of Universidad Nacional de La Plata, Argentina, for their support during his stay, where the model was developed and implemented. He also would like to thank Nancy Johnson for helpful discussions and Carina Verzi for corrections of this paper. Finally, the support from the organizing committee for the XIV Congress on Numerical Methods and their Applications, ENIEF 2004 and its Chairman, Gustavo Buscaglia is greatly appreciated.

References

[1] Barenblatt, G. I., 1962, "The Mathematical Theory of Equilibrium Cracks in Brittle Fracture," Adv. Appl. Mech., **7**, pp. 55–129.
[2] Dugdale, D. S., 1959, "Yielding of Steel Sheets Containing Slits," J. Mech. Phys. Solids, **8**, pp. 100–104.
[3] Tvergaard, V., and Hutchinson, J. W., 1992, "The Relation Between Crack Growth Resistance and Fracture Process Parameters in Elastic-Plastic Solids," J. Mech. Phys. Solids, **40**, pp. 1377–1397.
[4] Xu, X.-P., and Needleman, A., 1994, "Numerical Simulations of Fast Crack Growth in Brittle Solids," J. Mech. Phys. Solids, **42**(9), pp. 1397–1434.
[5] Camacho, G., and Ortiz, M., 1966, "Computational Modeling of Impact Damage in Brittle Materials," Int. J. Solids Struct., **33**, pp. 2899–2938.
[6] Espinosa, H. D., Zavattieri, P. D., and Dwivedi, S., 1998, "A Finite Deformation Continuum/Discrete Model for the Description of Fragmentation and Damage in Brittle Materials," J. Mech. Phys. Solids, **46**(10), pp. 1909–1942.
[7] Zavattieri, P. D., and Espinosa, H. D., 2001, "Grain Level Analysis of Ceramic Microstructures Subjected to Normal Impact Loading," Acta Mater., **49**(20), pp. 4291–4311.
[8] Klein, P. A., Foulk, J. W., Chen, E. P., Wimmer, S. A., and Gao, H., 2001, "Physics-Based Modeling of Brittle Fracture: Cohesive Formulations and the Application of Meshfree Methods," Theor. Appl. Fract. Mech., **37**(1–3), pp. 99–166.
[9] Moes, N., and Belytschko, T., 2002, "Extended Finite Element Method for Cohesive Crack Growth," Eng. Fract. Mech., **69**, pp. 813–833.
[10] De Borst, R., 2003, "Numerical Aspects of Cohesive-Zone Models," Eng. Fract. Mech., **70**(14), pp. 1743–1757.
[11] Ortiz, M., and Pandolfi, A., 1999, "Finite-Deformation Irreversible Cohesive Elements for Three-Dimensional Crack-Propagation Analysis," Int. J. Numer. Methods Eng., **44**, pp. 1267–1282.
[12] Pandolfi, A., Guduru, P. R., Ortiz, M., and Rosakis, A. J., 2000, "Three Dimensional Cohesive-Element Analysis and Experiments of Dynamic Fracture in C300 Steel," Int. J. Solids Struct., **37**, pp. 3733–3760.
[13] Zhou, F., and Molinari, J. F., 2004, "Dynamic Crack Propagation With Cohesive Elements: a Methodology to Address Mesh Dependency," Int. J. Numer. Methods Eng., **59**, pp. 1–24.
[14] Roychowdhury, S., Arun Roy, Y. D., and Dodds, R. H., Jr., 2002, "Ductile Tearing in Thin Aluminum Panels: Experiments and Analices Using Large-Displacement, 3-D Surface Cohesive Elements," Eng. Fract. Mech., **69**, pp. 983–1002.
[15] Belytschko, T., Liu, W. K., and Moran, B. G., 2000, *Nonlinear Finite Elements for Continua and Structures*, John Wiley & Sons, Ltd., New York.
[16] Li, W., and Siegmund, T., 2002, "An Analysis of Crack Growth in Thin-Sheet Metal via a Cohesive Zone Model," Eng. Fract. Mech., **69**(18), pp. 2073–2093.
[17] Cirak, F., Ortiz, M., and Pandolfi, A., 2005, "A Cohesive Approach to Thin-Shell Fracture and Fragmentation," Comput. Methods Appl. Mech. Eng., **194**(21–24), pp. 2604–2618.
[18] Belytschko, T., 1984, "Explicit Algorithms for Nonlinear Dynamics of Shells," Comput. Methods Appl. Mech. Eng., **43**, pp. 251–276.
[19] Lin, J., 1998, "DYNA3D: A Nonlinear, Explicit, Three-Dimensional Finite Element Code for Solid and Structural Mechanics. User Manual," MDGME, LLNL.
[20] Mindlin, R. D., 1951, "Influence of Rotary Inertia and Shear on Flexural Motions of Isotropic, Elastic Plates," ASME J. Appl. Mech., **18**, pp. 31–38.
[21] Rice, J. R., and Levy, N., 1972, "The Part-Through Surface Crack in an Elastic Plate," ASME J. Appl. Mech., **39**, pp. 185–194.
[22] Parks, D. M., and White, C. S., 1982, "Elastic-Plastic Line-Spring Finite-Elements for Surface-Cracked Plates and Shells," ASME J. Pressure Vessel Technol., **104**, pp. 287–292.
[23] Gullerud, A. S., Dodds, R. H. Jr., Hampton, R. W., and Dawicke, D. S., 1999, "Three-Dimensional Modeling of Dutile Crack Growth in Thin Sheet Metals: Computational Aspects and Validation," Eng. Fract. Mech., **63**, pp. 347–374.

[24] Rice, R. J., 1980, "The Mechanics of Earthquake Rupture," in *Physics of the Earth's Interior*, A. M. Dziewonski and E. Boschi, eds., Italian Physical Society/North-Holland Publ. Co, Amsterdam, pp. 555–649.
[25] Mahgoub, E., Deng, X., and Sutton, M. A., 2003, "Three-Dimensional Stress and Deformation Fields Around Flat and Slant Cracks Under Remote Mode I Loading Conditions" Eng. Fract. Mech., **70**(18), pp. 2527–2542.
[26] Chen, C. R., Kolednik, O., Scheider, I., Siegmund, T., Tatschl, A., and Fischer, F. D., 2003, "On the Determination of the Cohesive Zone Parameters for the Modeling of Micro-Ductile Crack Growth in Thick Specimens," Int. J. Fract., **120**, pp. 517–536.
[27] Chen, C. R., and Kolednik, O., 2005, "Comparison of Cohesive Zone Parameters and Crack Tip Stress States Between Two Different Specimen Types," Int. J. Fract., **132**, pp. 135–152.
[28] Chen, C. R., Kolednik, O., Heerens, J., and Fischer, F. D., 2005, "Three-Dimensional Modeling of Ductile Crack Growth: Cohesive Zone Parameters and Crack Tip Triaxility," Eng. Fract. Mech., **72**(13), pp. 2072–2094.
[29] Kwon, S. W., and Sun, C. T., 2000, "Characteristics of Three-Dimensional Stress Fields in Plates With a Though-the-Thickness Crack," Int. J. Fract., **104**, pp. 291–315.
[30] Mathur, K. K., Needleman, A., and Tvergaard, V., 1996, "Three Dimensional Analysis of Dynamic Ductile Crack Growth in a Thin Plate," J. Mech. Phys. Solids, **44**(3), pp. 439–464.